Supplementary information:

Barrett *et al.*, "Extra permeability is required to model dynamic oxygen measurements: evidence for functional recruitment?", JCBFM

Supplementary Methods

Nondimensionalization

The equations in the main text are non-dimensionalized to simplify the system and improve numerical stability using the same approach as our previous model (Barrett et al., 2012). The variables were scaled such that

$$\begin{aligned} c_{O_2,i}(t) &= C_{O_2,i}(T)/\hat{C}_{O_2}; \quad cmr_{O_2}(t) = CMR_{O_2}(T)/\hat{J}_{O_2}; \\ f_i(t) &= F_i(T)/\hat{F}; \qquad\qquad g_i = G_i/\hat{G}; \\ j_{O_2,i}(t) &= J_{O_2,i}(T)/\hat{J}_{O_2}; \qquad n_{O_2}(t) = N_{O_2}(T)/\hat{N}_{O_2}; \\ p_{O_2,i}(t) &= P_{O_2,i}(T)/\hat{P}_{O_2}; \qquad\qquad t = T/\hat{T}; \\ v_i(t) &= V_i(T)/\hat{V}; \qquad\qquad v_t = V_t/\hat{V}. \end{aligned} \tag{S.1}$$

We defined the scales as

$$\begin{aligned} \hat{C}_{O_2} &= C_{O_2,ref}; \qquad \hat{F} = F^*; \qquad \hat{G} = \hat{N}_{O_2}/\hat{P}_{O_2}\hat{T}; \\ \hat{J}_{O_2} &= \hat{N}_{O_2}/\hat{T}; \qquad \hat{N}_{O_2} = \hat{C}_{O_2}\hat{V}; \qquad \hat{P}_{O_2} = P_{O_2,ref}; \\ \hat{T} &= \hat{V}/\hat{F}; \qquad \text{and } \hat{V} = \textstyle\sum_{i=1}^{3} V_i^* \end{aligned} \tag{S.2}$$

where $C_{O_2,ref}$ and $P_{O_2,ref}$ are reference values for oxygen concentration and partial pressure, F^* is the flow at baseline, and $\sum_{i=1}^{3} V_i^*$ is the total volume of the three compartments at baseline. Derived variables or parameters not specifically mentioned in Equation (S.1) are nondimensionalized using the scale with the correct dimensions.

$CMRO_2$ Stimulus

The $CMRO_2$ stimulus, $s_t(t)$, is described by the piecewise function

$$s_t(t) = \begin{cases} s_{up}(t), & t < t_0 + \tau_{up} \\ s_{decay}(t), & t_0 + \tau_{up} \le t \le t_0 + t_{stim} \\ s_{down}(t), & t > t_0 + t_{stim} \end{cases} \tag{S.3}$$

where:

$$s_{up}(t) = \frac{1}{2} s^*_{up} \left[1 + \operatorname{erf}\left(\frac{t - [t_0 + \tau_{up}/2]}{32^{-1/2}\tau_{up}} \right) \right]; \tag{S.4a}$$

$$s_{decay}(t) = \left(s^*_{up} - s^* \right) \exp\left(\frac{t_0 + \tau_{up} - t}{\tau_{decay}} \right) + s^*; \tag{S.4b}$$

$$s_{down}(t) = s_{end} \exp\left(\frac{t_0 + t_{stim} - t}{\tau_{down}} \right); \tag{S.4c}$$

t_0 is the stimulus onset time; τ_X are time constants (where X is one of *up*, *decay*, or *down*); t_{stim} is the duration of stimulation (where $t_{stim} \geq \tau_{up}$); s^*_{up} is the peak value of $s_{up}(t)$; erf is the Gauss error function:

$$\operatorname{erf}(x) = \frac{2}{\sqrt{\pi}} \int_0^x \exp\left(-t^2\right) dt; \tag{S.5}$$

s^* is the steady state value of the stimulus; and s_{end}, the stimulus value at t_{end}, is given by $s_{decay}(t_{end})$.

To fit model predictions of tissue PO_2 to experimental measurements, the optimization algorithm adjusted the three stimulus time constants (τ_{up}, τ_{down}, and τ_{decay}) and two stimulus amplitudes (s^*_{up}, s^*), as described in the Methods section in the main text (Experimental Design subsection).

Calculating Mean Tissue PO_2

This section describes how the model calculates PO_2 in tissue, and provides the basis for calculating the value of baseline tissue PO_2 (see below). Although using an assumed or estimated PO_2 value would partially remove the need for this additional modelling, we believe that the equations in this section represent a more rigorous approach. As a consequence, the predictions in the main text do not depend on the details of the following model, but do rely on the baseline PO_2 value it produces.

While including these equations adds an additional layer of complexity, there are a number of advantages of doing so. For example, this technique makes it possible to estimate baseline tissue PO_2 using the radial measurements of tissue PO_2 made by Vovenko (1999), whose vascular PO_2 mea-

surements define the model's reference state (see below). In addition, this approach allows us to predict the dynamic PO_2 of tissue with a baseline PO_2 value different to the average, as discussed below. For brevity, the notation used for most of this section is different to that of the main text.

Oxygen transport in an annular slice of tissue of radius R_2 surrounding a blood vessel of radius R_1 can be described by the differential equation

$$\frac{1}{r}\frac{d}{dr}\left(r\frac{dp}{dr}\right) = \frac{m}{D} \tag{S.6}$$

where r is the radial co-ordinate, $p(r)$ is the oxygen partial pressure, and the constants m and D are the tissue consumption rate and diffusivity of oxygen, respectively. Solving this equation subject to the boundary conditions

$$p(R_1) = p_b; \quad \left.\frac{dp}{dr}\right|_{r=R_2} = 0 \tag{S.7}$$

leads to

$$p(r) = p_b + \frac{m}{4D}\left(r^2 - R_1^2\right) - \frac{mR_2^2}{2D}\ln\frac{r}{R_1}, \tag{S.8}$$

where the constant p_b is the PO_2 in the blood vessel.

Making the substitution $k = \frac{m}{D}$ and applying the additional constraint $p(R_2) = p_{t0}$, where p_{t0} is the lowest partial pressure in the tissue, Equation (S.8) becomes

$$p(r) = p_b + \frac{1}{4}k\left(r^2 - R_1^2\right) - \frac{1}{2}kR_2^2\ln\frac{r}{R_1}, \tag{S.9}$$

where

$$k = (p_{t0} - p_b)/\alpha \tag{S.10}$$

and

$$\alpha = \frac{1}{4}\left(R_2^2 - R_1^2\right) - \frac{1}{2}R_2^2\ln\frac{R_2}{R_1}. \tag{S.11}$$

The average PO_2 in the tissue area, $\bar{p}$, can be calculated by substituting

Equation (S.9) into the integral

$$\bar{p} = \frac{\int_{R_1}^{R_2} rp(r)dr}{\int_{R_1}^{R_2} rdr}, \tag{S.12}$$

and solving analytically (by parts) to obtain

$$\bar{p} = p_b + \frac{1}{8}k\frac{R_2^4 - R_1^4}{R_2^2 - R_1^2} + \frac{1}{4}k\left(R_2^2 - R_1^2\right) - \frac{1}{2}k\frac{R_2^4}{R_2^2 - R_1^2}\ln\frac{R_2}{R_1}. \tag{S.13}$$

Equation (S.13) can also be written as a weighted sum of the two boundary partial pressures, such that

$$\bar{p} = w_b p_b + (1 - w_b)p_{t0} \tag{S.14}$$

where w_b, the weight applied to the oxygen partial pressure in the blood, is given by

$$w_b = 1 - \frac{R_2^4 - R_1^4}{8\alpha\left(R_2^2 - R_1^2\right)} - \frac{1}{4\alpha}\left(R_2^2 - R_1^2\right) + \frac{R_2^4}{2\alpha\left(R_2^2 - R_1^2\right)}\ln\frac{R_2}{R_1}. \tag{S.15}$$

For a tissue compartment made up of three of the annuli described by the preceding equations, the average oxygen partial pressure, $\bar{p}_t$, can be written as a weighted sum of the individual compartment averages such that

$$\bar{p}_t = \sum_{i=1}^{3} w_i' \bar{p}_i, \tag{S.16}$$

where w_i' is the weight applied to compartment i (weights must sum to 1), and $\bar{p}_i$ is the average partial pressure, which is calculated from Equation (S.14). We used the baseline vascular volume fractions, v_i^*, as compartment weights (w_i'). For simplicity, we assumed constant radii (R_1 and R_2) in the different vascular compartments. On the basis of recent evidence from two-photon microscopy (Devor et al., 2011), we assumed the minimum PO_2 was the same for tissue surrounding each of the vascular compartments. As such, Equation (S.16) can also be written in terms of the vascular PO_2 and

the minimum PO_2 in the tissue so

$$\bar{p_t} = w_{t0} p_{t0} + \sum_{i=1}^{3} w_i p_{bi}, \tag{S.17}$$

where $w_i = w_i' w_b$, $w_{t0} = 1 - \sum_{i=1}^{3} w_i$, and p_{bi} are the boundary partial pressures in the three vascular (blood) compartments. Using the same notation as the main text, Equation (S.17) would be written as

$$\bar{p}_{O_2,t}(t) = w_{t0} p_{O_2,t0}(t) + \sum_{i=1}^{3} w_i \bar{p}_{O_2,i}(t) \tag{S.18}$$

Parameter Selection and Solution Procedure

This section gives more detail on the choice of parameters used in the model, and how the equations were solved to produce the predictions in the results section. Equation numbers not prefaced by 'S' refer to equations in the main text. Supplementary Table 1 summarizes the parameter values, with more detail given below.

In brief, the model was solved in three stages: 1) calculating the full set of parameters in a reference state; 2) adjusting the baseline parameters to account for experimental conditions different from the reference state (discussed in the next subsection); and 3) numerically solving the equations to produce the dynamic results. We chose to use the conditions observed by Vovenko (1999) as a reference state for the model, since these data provided nearly all of the measurements required to parametrize the model.

To determine the dimensionless tissue volume, we calculated the mean vascular volume fraction (2.87%) from data reported by a range of groups with different methodologies (An and Lin, 2002; Ito et al., 2005, 2001; Kim et al., 2007; Lauwers et al., 2008; Reichold et al., 2009; Weber et al., 2008). Since we scale volume terms by the total baseline vascular volume (Barrett et al., 2012), this means the dimensionless tissue volume, v_t, becomes 34.8.

First, we set $[R_1, R_2] = [15, 135]$ μm on the basis of recent measurements of radial PO_2 in tissue (Devor et al., 2011), and included modifications to

these parameters in the sensitivity analysis. Next, to determine the baseline value for the minimum tissue PO_2, ${p_{O_2,t0}}^*$, we fit the model described in Equation (S.9) to radial measurements of tissue PO_2 in all three vascular compartments (Vovenko, 1999). Then, we used measurements of vascular PO_2 (Vovenko, 1999) to calculate baseline O_2 concentrations (${c_{O_2,i,i+1}}^*$) from Equation (7), baseline O_2 amounts (${n_{O_2,i,i+1}}^*$) and the leak concentration ($c_{O_2,l}$) from Equation (3), and average vascular PO_2 (${\bar{p}_{O_2,i}}^*$) from Equation (6). This makes it possible to calculate the average tissue PO_2 (${\bar{p}_{O_2,t}}^*$) from Equation (S.18). The baseline oxygen consumption, $cmr^*_{O_2}$, was calculated from Equation (2).

We identified a feasible range of values for the shunt conduction coefficient, g_s, by requiring all conduction coefficients to be greater than zero to ensure that O_2 diffuses down its partial pressure gradient. The steady state forms of equations (1a) and (1c) then yield two inequalities that define the feasible range for g_s. Initial simulations (data not shown) suggested that the dynamics of PO_2 were not particularly sensitive to the value of g_s, so we defined g_s as the mean of the feasible range, but included values at the top and bottom 10% of the range in the sensitivity analysis. The remaining conduction coefficients were determined by solving Equations (1) at steady state. At this point, the model is fully parametrized in the reference state.

Adjusting Baseline Conditions

This section describes the process of adjusting the parameters from the reference state conditions to the conditions under which the other data sets were obtained. All of the parameters adjusted under these different experimental conditions are listed in Supplementary Table 2.

To adjust the model from the reference state to the conditions reported by Masamoto et al. (2008), we changed only the value for femoral artery PO_2 ($p_{O_2,0}$) as no other vascular PO_2 measurements were reported. As such, we assumed that baseline $CMRO_2$ ($cmr^*_{O_2}$) and the O_2 conduction coefficients (g and g_s) were unchanged from the reference state. This means the steady state version of Equations (1) and (2) can be solved directly for the new

baseline conditions.

For the simulations of data from Yaseen et al. (2011) and Vazquez et al. (2010), we adjusted the femoral artery PO_2 ($p_{O_2,0}$), large venous PO_2 ($p_{O_2}{}^*_{,3,4}$), and average venous PO_2 ($\bar{p}_{O_2,3}{}^*$) to match the reported measurements (see Table 2 in the main text). For all simulations, the concentration of oxygen 'leaked' between the femoral artery and large cerebral arteries, $c_{O_2,l}$, remained constant. Adding the steady state form of Equations (1) and (2), the adjusted baseline $CMRO_2$ is obtained such that

$$cmr^*_{O_2} = f^* \left(c_{O_2}{}^*_{,0,1} - c_{O_2}{}^*_{,3,4} \right), \tag{S.19}$$

where f^* is the baseline CBF, and $c_{O_2}{}^*_{,0,1}$ and $c_{O_2}{}^*_{,3,4}$ are the baseline input arterial and output venous oxygen concentrations calculated from the imposed PO_2 values.

In both cases, the baseline state is underdetermined: the steady state form of Equations (1) and (2) provide 3 equations to determine 6 unknowns (g, g_s, $p_{O_2}{}^*_{,1,2}$ and $\bar{p}_{O_2,t}{}^*$). Therefore, it was necessary to make one or more assumptions about the baseline conditions. We describe the particular assumption used in more detail below, but during development we tested a number of plausible assumptions, which gave mostly similar results since the input (femoral artery PO_2) and output (large venous PO_2) values were defined by experimental data.

To determine the O_2 conduction coefficients we assumed that, for the same femoral artery PO_2, the proportion of $CMRO_2$ supplied by each compartment at baseline would be constant between different experimental conditions. For example, for the conditions reported by Vazquez et al. (2010), we assumed that the steady state fraction of total oxygen flux supplied by each vascular compartment would be the same as those under the reference state conditions, if the femoral artery PO_2 was reduced to that of the reference state (Vovenko, 1999) while maintaining the newly-calculated $CMRO_2$.

Since $CMRO_2$ remains constant between these two conditions, the output venous O_2 concentration under the reference femoral artery PO_2 conditions, $\acute{c}_{O_2}{}^*_{,3,4}$, can be calculated from a modified form of Equation (S.19)

as

$$\acute{c}_{O_2,3,4}^{*} = \acute{c}_{O_2,0,1}^{*} - cmr_{O_2}^{*}/f^{*}. \tag{S.20}$$

Then, $\acute{p}_{O_2,3,4}^{*}$ can be calculated from $\acute{c}_{O_2,3,4}^{*}$ using Equation (7).

This leaves a system of 6 equations (the previously mentioned 3, plus the steady state form of Equations (1) and (2) under the reference femoral artery PO_2 conditions) and 9 unknowns (the previously mentioned 6, plus $\acute{p}_{O_2,1,2}^{*}$, $\acute{p}_{O_2,2,3}^{*}$, and $\acute{\bar{p}}_{O_2,t}^{*}$). The final 3 equations come from the assumption of constant fractional O_2 supply from each compartment, such that

$$\frac{g_i\left(\acute{\bar{p}}_{O_2,i}^{*} - \acute{\bar{p}}_{O_2,t}^{*}\right)}{cmr_{O_2}^{*}} = k_{O_2,i}, \tag{S.21}$$

where the constant $k_{O_2,i}$ is the proportion of $CMRO_2$ supplied from the compartment, and is calculated from the reference conditions. This assumption requires that the shunt conduction coefficient (g_s) be free to deviate from the mean of the feasible range; however, the value was determined to be within $\sim 10\%$ of the mean.

Finally, with the adjusted parameters fully specified, the four ordinary differential equations specified in Equations (1) and (2) were solved numerically to produce the dynamic predictions.

Adjusting Tissue PO_2 Predictions

The methods section in the main text outlines the principle behind adjusting the tissue PO_2 predictions and the rationale for doing so. However, in practice there are five steps required to produce these additional predictions.

First, the mean baseline tissue PO_2, $\bar{p}_{O_2,t}{}^{*}$, is calculated by adjusting the reference state for different experimental conditions, as described in the previous section. Second, we choose new weights, $w_x^{\star}$, to satisfy the equation

$$p_{O_2,t}^{\star} = w_{t0}^{\star} p_{O_2,t0}{}^{*} + \sum_{i=1}^{3} w_i^{\star} \bar{p}_{O_2,i}{}^{*}, \tag{S.22}$$

where $p_{O_2,t}^{\star}$ is the measured tissue PO_2 at baseline. The new weights must

sum to one, but since Equation (S.22) is still underconstrained, the new weights are calculated by minimising the change from the original weights (i.e. $w_x^\star - w_x$).

Third, the dynamic mean tissue PO_2, $\bar{p}_{O_2,t}(t)$, is calculated by solving the ordinary differential equations in the main text, as discussed in the previous section. Fourth, the minimum tissue PO_2, $p_{O_2,t0}(t)$, is calculated by rearranging Equation (S.18). Finally the additional dynamic tissue PO_2 prediction is calculated from

$$p_{O_2,t}^\star(t) = w_{t0}^\star p_{O_2,t0}(t) + \sum_{i=1}^{3} w_i^\star \bar{p}_{O_2,i}(t). \tag{S.23}$$

In this way it is possible to estimate the dynamic PO_2 of tissue with any baseline value between the minimum tissue value, ${p_{O_2,t0}}^*$, and the maximum vascular (arterial) value, ${\bar{p}_{O_2,1}}^*$.

Steps three, four, and five are repeated during each iteration of the optimisation in order to determine the $CMRO_2$ parameters that generate the best fit between Equation (S.23) and the experimental observations. However, the new weights, $w_x^\star$, are only calculated once to match the model-predicted and measured baseline tissue PO_2, and are not used as fitting parameters in the dynamic simulations.

Supplementary References

An, H. and Lin, W. (2002). Cerebral venous and arterial blood volumes can be estimated separately in humans using magnetic resonance imaging. *Magn. Reson. Med.*, 48(4):583–588.

Attwell, D., Buchan, A. M., Charpak, S., Lauritzen, M., MacVicar, B. A., and Newman, E. A. (2010). Glial and neuronal control of brain blood flow. *Nature*, 468(7321):232–243.

Barrett, M. J., Tawhai, M. H., and Suresh, V. (2012). Arteries dominate volume changes during brief functional hyperemia: Evidence from mathematical modelling. *NeuroImage*, 62(1):482 – 492.

Buxton, R. B., Uludag, K., Dubowitz, D. J., and Liu, T. T. (2004). Modeling the hemodynamic response to brain activation. *Neuroimage*, 23(Supplement 1):S220 – S233.

Cartheuser, C.-F. (1993). Standard and ph-affected hemoglobin-o2 binding curves of sprague-dawley rats under normal and shifted p50 conditions. *Comp. Biochem. Physiol. A.*, 106(4):775 – 782.

Dash, R. and Bassingthwaighte, J. (2004). Blood hbo2 and hbco2 dissociation curves at varied o2, co2, ph, 2,3-dpg and temperature levels. *Ann. Biomed. Eng.*, 32(12):1676–1693.

Devor, A., Sakadžić, S., Saisan, P. A., Yaseen, M. A., Roussakis, E., Srinivasan, V. J., Vinogradov, S. A., Rosen, B. R., Buxton, R. B., Dale, A. M., and Boas, D. A. (2011). "overshoot" of o2 is required to maintain baseline tissue oxygenation at locations distal to blood vessels. *J. Neurosci.*, 31(38):13676–13681.

Ito, H., Ibaraki, M., Kanno, I., Fukuda, H., and Miura, S. (2005). Changes in the arterial fraction of human cerebral blood volume during hypercapnia and hypocapnia measured by positron emission tomography. *J. Cereb. Blood Flow Metab.*, 25(7):852–857.

Ito, H., Kanno, I., Iida, H., Hatazawa, J., Shimosegawa, E., Tamura, H., and Okudera, T. (2001). Arterial fraction of cerebral blood volume in humans measured by positron emission tomography. *Ann. Nucl. Med.*, 15:111–116.

Kim, T., Hendrich, K. S., Masamoto, K., and Kim, S.-G. (2007). Arterial versus total blood volume changes during neural activity-induced cerebral blood flow change: implication for bold fmri. *J. Cereb. Blood Flow Metab.*, 27(6):1235–1247.

Lagarias, J. C., Reeds, J. A., Wright, M. H., and Wright, P. E. (1998). Convergence properties of the nelder–mead simplex method in low dimensions. *SIAM Journal on Optimization*, 9(1):112–147.

Lauwers, F., Cassot, F., Lauwers-Cances, V., Puwanarajah, P., and Duvernoy, H. (2008). Morphometry of the human cerebral cortex microcirculation: General characteristics and space-related profiles. *Neuroimage*, 39(3):936 – 948.

Lecoq, J., Parpaleix, A., Roussakis, E., Ducros, M., Houssen, Y. G., Vinogradov, S. A., and Charpak, S. (2011). Simultaneous two-photon imaging of oxygen and blood flow in deep cerebral vessels. *Nature Medicine*, 17(7):893–898.

Masamoto, K., Vazquez, A., Wang, P., and Kim, S.-G. (2008). Trial-by-trial relationship between neural activity, oxygen consumption, and blood flow responses. *Neuroimage*, 40(2):442 – 450.

Reichold, J., Stampanoni, M., Lena Keller, A., Buck, A., Jenny, P., and Weber, B. (2009). Vascular graph model to simulate the cerebral blood flow in realistic vascular networks. *J. Cereb. Blood Flow Metab.*, 29(8):1429–1443.

Vazquez, A. L., Fukuda, M., Tasker, M. L., Masamoto, K., and Kim, S.-G. (2010). Changes in cerebral arterial, tissue and venous oxygenation with evoked neural stimulation: implications for hemoglobin-based functional neuroimaging. *J. Cereb. Blood Flow Metab.*, 30(2):428–439.

Vovenko, E. (1999). Distribution of oxygen tension on the surface of arterioles, capillaries and venules of brain cortex and in tissue in normoxia: an experimental study on rats. *Pflugers Arch.*, 437(4):617–623.

Weber, B., Keller, A. L., Reichold, J., and Logothetis, N. K. (2008). The microvascular system of the striate and extrastriate visual cortex of the macaque. *Cereb. Cort.*, 18(10):2318–2330.

Yaseen, M. A., Srinivasan, V. J., Sakadzic, S., Radhakrishnan, H., Gorczynska, I., Wu, W., Fujimoto, J. G., and Boas, D. A. (2011). Microvascular oxygen tension and flow measurements in rodent cerebral cortex during baseline conditions and functional activation. *J Cereb Blood Flow Metab*, 31(4):1051–1063.

Supplementary Table 1: List of model parameters in the reference state. Parameters with three values represent $x = [x_1, x_2, x_3]$. Parameters with lower case symbols are dimensionless (see the Supplementary Methods), while parameters with upper case symbols are not and are given with appropriate units.

Symbol	Description	Value	Reference
$C_{O_2,l}$	O_2 conc. leakage	0.116 mM	See Supplementary Methods
$C_{O_2,max}$	Hill equation max. O_2 conc.	9.26 mM	Cartheuser (1993)
prop(g_s)	Proportion of shunt feasible range	50%	See Supplementary Methods
h	Hill equation exponent	2.6	Cartheuser (1993)
P_{50}	Hill equation O_2 P_{50}	36 mmHg	Cartheuser (1993)
ΔP_{SNP}	SNP-induced pressure drop	50%	Masamoto et al. (2008)
$[R_1, R_2]$	Krogh cylinder radii	[15, 135] μm	See Supplementary Methods
v^*	Baseline vascular volume fraction	[0.29, 0.44, 0.27]	Barrett et al. (2012)
v_t	Tissue volume fraction	34.8	See Supplementary Methods
w_b	Vascular PO_2 weight	0.133	See Supplementary Methods
w_i'	Vascular compartment weight	v^*	See Supplementary Methods
σ_{O_2}	Tissue O_2 solubility coefficient	1.46 μM/mmHg	Dash and Bassingthwaighte (2004)

Supplementary Table 2: List of adjusted model parameters for simulations of experimental conditions (see Table 2 in the main text). Values give by '-' are the same as the reference state (Vovenko).

Symbol	Description	Unit	Value for simulations of:			
			Vovenko (1999)	Yaseen (2011)	Masamoto (2008)	Vazquez (2010)
$P_{O_2,0,1}^{*}$	Baseline input art. PO_2	mmHg	81.2	99.4	103.7	116.7
$P_{O_2,1,2}^{*}$	Baseline art.–cap. PO_2	mmHg	59.7	68.0	62.3	55.7
$P_{O_2,2,3}^{*}$	Baseline cap.–vei. PO_2	mmHg	39.6	50.1	41.1	35.3
$P_{O_2,3,4}^{*}$	Baseline output vei. PO_2	mmHg	41.3	54.4	44.6	40.3
$\bar{P}_{O_2,t}{}^{*}$	Mean baseline tis. PO_2	mmHg	22.4	38.1	25.3	22.8
$cmr_{O_2}^{*}$	Baseline $CMRO_2$	none	0.336	0.208	-	0.423
g_1	Art. O_2 conduction coef.	none	0.075	0.059	-	0.096
g_2	Cap. O_2 conduction coef.	none	0.790	0.619	-	1.124
g_3	Vei. O_2 conduction coef.	none	0.201	0.155	-	0.309
g_s	Shunt O_2 conduction coef.	none	0.207	0.198	-	0.263

Supplementary Table 3: List of parameters modified in the sensitivity analysis and the amount of perturbation imposed. For parameters with multiple values (e.g. ${p_{O_2}}^*$), each value was perturbed individually. Perturbations to the reference conditions also affect simulations under modified experimental conditions.

Data Set	Symbol	Perturbation
Reference	${p_{O_2}}^*$	±10%
	$[R_1, R_2]$	±10%
	prop(g_s)	±40%
	v^*	±10%
	v_t	±10%
Masamoto et al. (2008)	ΔP_{SNP}	±10%
	$p^*_{O_2,0}$	±10%
Vazquez et al. (2010)	$p^*_{O_2,0}$	±10%
	$p^*_{O_2,3,4}$	±5%
	$\bar{p}^*_{O_2,3}$	±5%

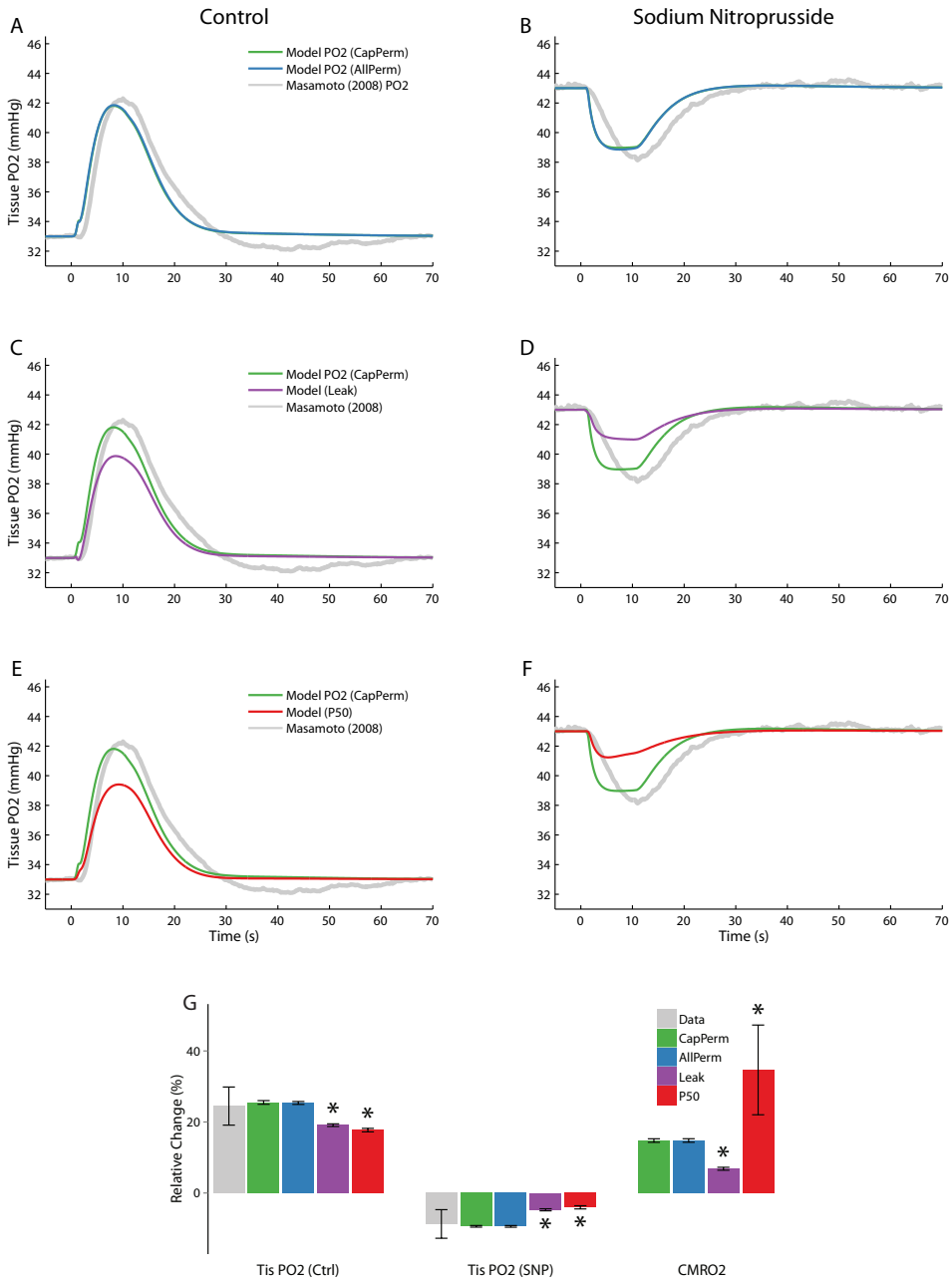

Supplementary Figure 1: Model predictions (with additional mechanisms) of data from Masamoto et al. (2008) in response to 10s electrical forepaw stimulation. Format as per Figure 3 in the main text.

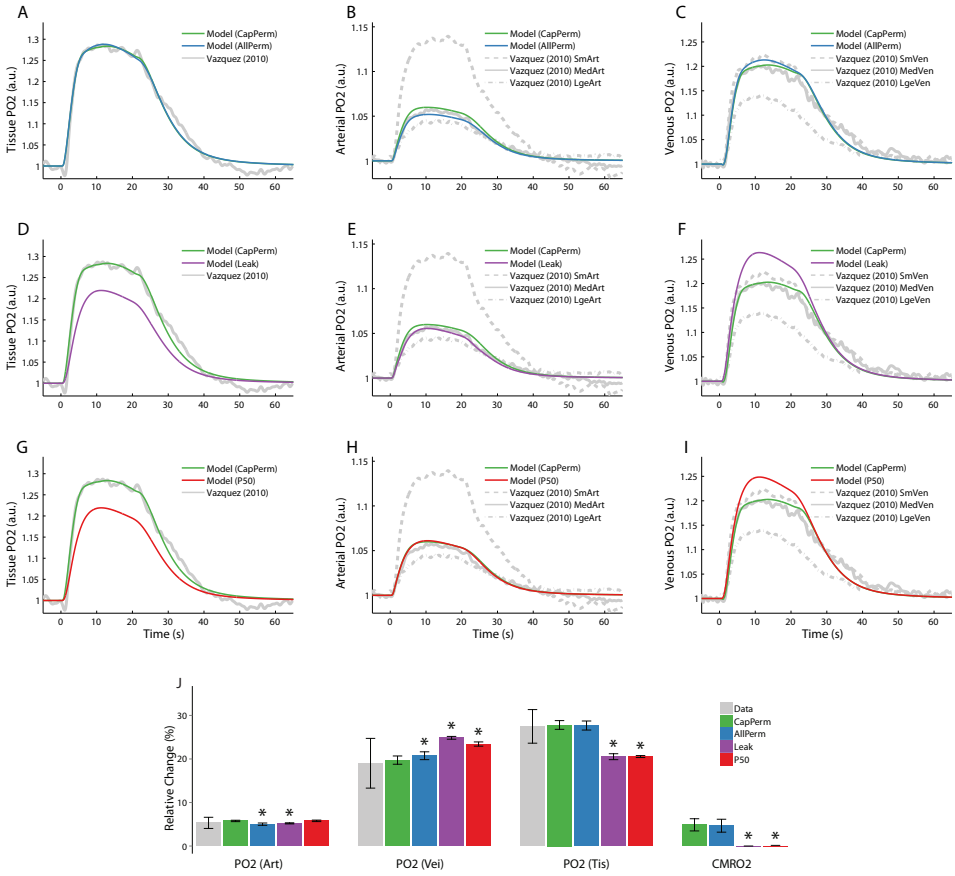

Supplementary Figure 2: Model predictions (with additional mechanisms) of data from Vazquez et al. (2010) in response to 20s electrical forepaw stimulation. Format as per Figure 4 in the main text.